Chinese Chemical Letters 33 (2022) 1236–1244

Contents lists available at ScienceDirect

Chinese Chemical Letters

journal homepage: www.elsevier.com/locate/cclet

# Strategies for constructing manganese-based oxide electrode materials for aqueous rechargeable zinc-ion batteries

Ying Liu[a], Xiang Wu[a,b,c,*]

[a] School of Materials Science and Engineering, Shenyang University of Technology, Shenyang 110870, China
[b] State Key Laboratory of High-Performance Ceramics and Superfine Microstructure, Shanghai Institute of Ceramics, Chinese Academy of Sciences, Shanghai 200050, China
[c] State Key Laboratory of Metastable Materials Science and Technology, Yanshan University, Qinhuangdao 066004, China

ARTICLE INFO

*Article history:*
Received 17 July 2021
Revised 12 August 2021
Accepted 18 August 2021
Available online 23 August 2021

*Keywords:*
Aqueous zinc ion batteries
Mn-based compounds
Cathode materials
$MnO_2$
Secondary batteries

ABSTRACT

Commercial lithium-ion batteries (LIBs) have been widely used in various energy storage systems. However, many unfavorable factors of LIBs have prompted researchers to turn their attention to the development of emerging secondary batteries. Aqueous zinc ion batteries (AZIBs) present some prominent advantages with environmental friendliness, low cost and convenient operation feature. $MnO_2$ electrode is the first to be discovered as promising cathode material. So far, manganese-based oxides have made significant progresses in improving the inherent capacity and energy density. Herein, we summarize comprehensively recent advances of Mn-based compounds as electrode materials for ZIBs. Especially, this review focuses on the design strategies of electrode structures, optimization of the electrochemical performance and the clarification of energy storage mechanisms. Finally, their future research directions and perspective are also proposed.



## 1. Introduction

The storage and conversion of energy sources is an important step to achieve sustainable development with future carbon neutralization policy [1–4]. LIBs with high energy density are widely employed in various fields. But the expensive and flammable disadvantages hinder their practical applications [5–7]. Considering the issues of safety and cost, rechargeable aqueous metal ion batteries (Li, Na, K, Zn, Mg and Al) might be an alternative to LIBs [8–12]. Fig. 1a shows the characteristics of organic and aqueous electrolytes in metal ion batteries. It is found that the former possesses the characteristic of flammability with high risk. On the contrary, the latter presents high safety and ionic conductivity up to $10^{-1}$-6 S/cm. In terms of metal anode materials, the radii of monovalent ions ($Na^+$ and $K^+$) and multivalent ions ($Mg^{2+}$) are much larger than that of $Li^+$. It indicates that the above batteries present slow kinetics and poor cycling stability. Although Al electrode material possesses a large specific capacity, the standard electrode potential of $Al^{3+}$/Al is very low [13]. Compared with the above mentioned metals, Zn presents small ionic radius (0.75 Å), suitable standard electrode potential (-0.763 V *vs.* SHE) and high stability (Fig. 1b).

Recently AZIBs have attracted widely attention due to their outstanding advantages [14–16]. So far, there are many reports about cathode materials for ZIBs, such as manganese-based (Mn-based) compounds [17–19], vanadium-based materials [20–23], Prussian blue analogs [24,25] and polyanion compounds [26,27]. Rechargeable Zn-$MnO_2$ battery was first discovered in 1986. Shoji and coworkers designed Zn-$MnO_2$ cells with 2 mol/L $ZnSO_4$ electrolyte, which opens a new path to develop AZIBs [28]. After that, a plenty of work has focused on polymorphic Mn-based compounds due to their non-toxicity, low cost and rich crystal structure [29–33]. In fact, the connection mode of $MnO_6$ octahedrons determines $MnO_2$ crystal structure, including $\alpha$-, $\beta$-, $\gamma$-, $\lambda$-, *R*-, $\delta$-, $\varepsilon$- and T-$MnO_2$. These structures can be mutually transformed and seriously affect their electrochemical performance (Fig. 2) [34–37]. In this review, we summarize the progress of Mn-based compounds in ZIBs, including electrode design, electrochemical performance and energy storage mechanism. The limitation and future perspective of ZIBs are also proposed.

## 2. Electrode structures

Mn is a common transition metal element with multiple oxidation states (+2, +3 and +4). As a cathode material for ZIBs, Mn-based compounds have been widely investigated in recent years. It is reported that $MnO_2$ possesses a theoretical capacity of 308

* Corresponding author.
*E-mail address:* wuxiang05@sut.edu.cn (X. Wu).

https://doi.org/10.1016/j.cclet.2021.08.081
1001-8417/

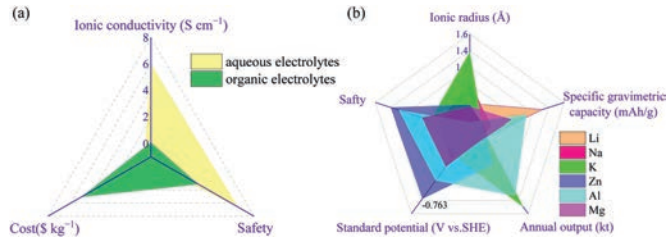


**Fig. 1.** (a) The advantages of organic and aqueous electrolyte in metal ion batteries. (b) Radar diagram of various metal ions.

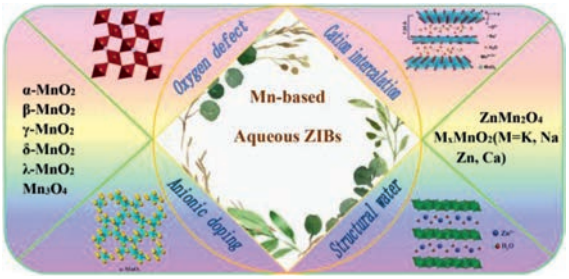


**Fig. 2.** Classification and synthesized strategies of Mn-based cathode for aqueous zinc ion batteries.

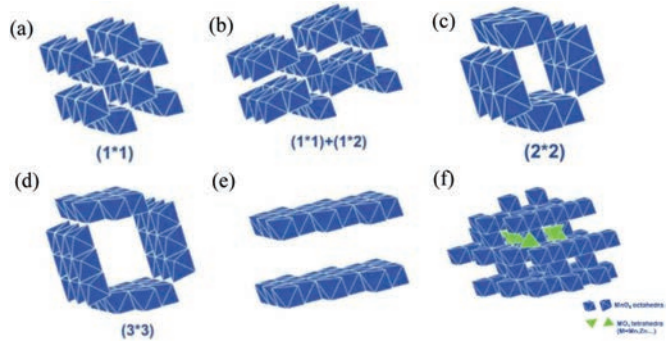


**Fig. 3.** Manganese oxide crystal structures (a) $\beta$-$MnO_2$ (pyrolusite-type), (b) $\gamma$-$MnO_2$(nsutite-type), (c) $\alpha$-$MnO_2$ (hollandite-type), (d) todorokite-type $MnO_2$, (e) $\delta$-$MnO_2$ (birnessite-type), (f) $\lambda$-$MnO_2$ (spinel-type). Reproduced with permission [8]. Copyright 2018, Wiley-VCH.

mAh/g and a voltage window of 0.8-1.8 V. In addition, $MnO_2$ materials present diverse crystallographic frameworks. The crystal structure can be classified into three categories: tunnel structure, spinel and layer structure, as shown in Fig. 3 [8].

### 2.1. Tunnel structure

$\beta$-$MnO_2$ (pyrolusite-type) with 1 × 1 tunnel is a frame structure formed by $MnO_6$ octahedrons assembling with sharing corners (Fig. 3a). In literature, $\beta$-$MnO_2$ cathode was synthesized through a hydrothermal route with a capacity of 355 mAh/g at 0.1 A/g [38]. Huang and co-workers prepared $\beta$-$MnO_2$ nanorods by introducing N element for improving the electrochemical performance of device. The results show that N-doping effectively enhances the conductivity of $MnO_2$ materials, as shown in Fig. 4a [39]. Oxygen vacancy ($V_o$) are an important defect, which can not only improve ion insertion kinetics, but also change the thermodynamics of electrode surface [40]. Zhou's group constructed $\beta$-$MnO_2$ with oxygen defects to improve electrode reaction activity and specific capacity (Fig. 4b). $V_o$-$\beta$-$MnO_2$-Zn battery delivers a discharge capacity of 302 mAh/g and capacity retention of 94% at 0.5 A/g after 300 cycles (Figs. 4c and d). Additionally, the device possesses low $R_{ct}$, indicating their excellent electrical conductivity [41]. Moreover, $V_o$ can cause rearrangement of surrounding atoms, resulting in a change in the electronic structure of metal oxides. The above methods are effective strategies (heteroatom doping and vacancy) to improve the conductivity of cathode and enable device to obtain fast ion insertion kinetics [42].

$\gamma$-$MnO_2$ materials with a mixed tunnel structure of 1 × 1 and 1 × 2 (Fig. 3b) was reported by Alfaruqi *et al*. through an environmental temperature strategy. BET results show that $\gamma$-$MnO_2$ electrode shows a total surface area of 148 $m^2$/g, and the pore size is 3.77 nm. This mesoporous electrode can provide a sufficient electrode/electrolyte contact area. In addition, the high surface area of electrode ensures easy insertion/de-embedding of $Zn^{2+}$. Surprisingly, when $Zn^{2+}$ is fully intercalated, tunnel type $\gamma$-$MnO_2$ transforms into spinel type $ZnMn_2O_4$ (ZMO), $\gamma$-$Zn_xMnO_2$ (tunnel type) and L-$Zn_yMnO_2$ (layered) phase. It shows $Mn^{4+}$ is reduced to $Mn^{3+}$ and $Mn^{2+}$. To be precise, a part of $\gamma$-$MnO_2$ undergoes the transformation to spinel ZMO in early stage of Zn insertion, as shown in Fig. 5.

In subsequent dezincification process, phase change of materials is almost completely restored to the original $\gamma$-$MnO_2$. Zn/$\gamma$-$MnO_2$ batteries show an initial discharge capacity of 285 mAh/g at 0.05 mA/$cm^2$. It indicated the mesoporous electrode can provide a large electrode/electrolyte contact area, thereby accelerating their diffusion kinetics [43]. The synergistic effect also can enhance the conductivity of electrode due to help of "external force" that the dissolution of $MnO_2$ is alleviated during reaction process. For instance, Lu's group utilized high conductivity of graphene to assemble a Zn//$\gamma$-$MnO_2$-graphene battery. Compared to bare $MnO_2$ electrode, $MnO_2$-graphene one shows excellent cycle stability. After 300 cycles, the cell maintains 64.1% of the initial capacity at 20 mA/$cm^2$, which is equivalent to a capacity decay rate of 0.12% per cycle. The increase in cycle stability can be attributed to the joint cooperation of graphene and $MnO_2$ [44].

$\alpha$-$MnO_2$ also possesses a tunnel structure, and each side of tunnel consists of two $MnO_6$ octahedrons, which is a 2 × 2 tunnel (Fig. 3c). Pan *et al.* reported Zn/$\alpha$-$MnO_2$ batteries with a significant attenuation in the first 10 cycles. However, the capacity retention is poor in subsequent cycles. It might be attributed to the dissolution of $Mn^{2+}$ into $ZnSO_4$ during cycling. Therefore, 0.1 mol/L $Mn^{2+}$ was pre-added in electrolyte to reach equilibrium with $Mn^{2+}$ dissolved phase. The results show that Zn/$MnO_2$ battery with $MnSO_4$ additive delivers a capacity retention rate of 92% after 5000 cycles at 5 C [45]. Wu's group designed a device using $\alpha$-$MnO_2$ /graphene scrolls as cathode. It presents a capacity of 362.2 mAh/g at 0.3 A/g. There is an inflection point located at 1.3 V in GCD curves (Fig. 6a). It means that the intercalation of Zn ions takes place in two stages. In the first stage of embedding, layer Zn-buserite is formed first. In the second stage, zinc ions are embedded in tunnel structure. Due to large electrostatic interaction at this stage, the electrode is in an unstable state. The coating of graphene scrolls on $MnO_2$ nanowire (MNW) improves the stability of electrode, and its rate performance is also significantly enhanced (Fig. 6b). Moreover, it is beneficial to alleviating the dissolution of Mn element during discharge, as shown in Fig. 6c [46].

Pre-embedding of large cations can stabilize the tunnel structured $MnO_2$ *via* the coordination of guest ions with adjacent atoms. For instance, Liu and co-workers designed $\alpha$-$MnO_2$ and $\alpha$-$K_{0.19}MnO_2$ structures by a self-sacrificing template method. After annealing, the shell of $\alpha$-$K_{0.19}MnO_2$ nanotubes changed from a nanosheet to a vertical uniform nanorod to form a porous structure (Fig. 6d). This highly porous structure facilitates full contact with electrolyte. Furthermore, after $K^+$ enters the tunnel cavity, they possess an interplanar spacing of 0.693 nm as shown in Fig. 6e. The pre-intercalated K ions enter the framework of electrode as pillars, which prevent the structure from collapsing during long cycles (Fig. 6f). Apart from this, enough tunnel space can speed

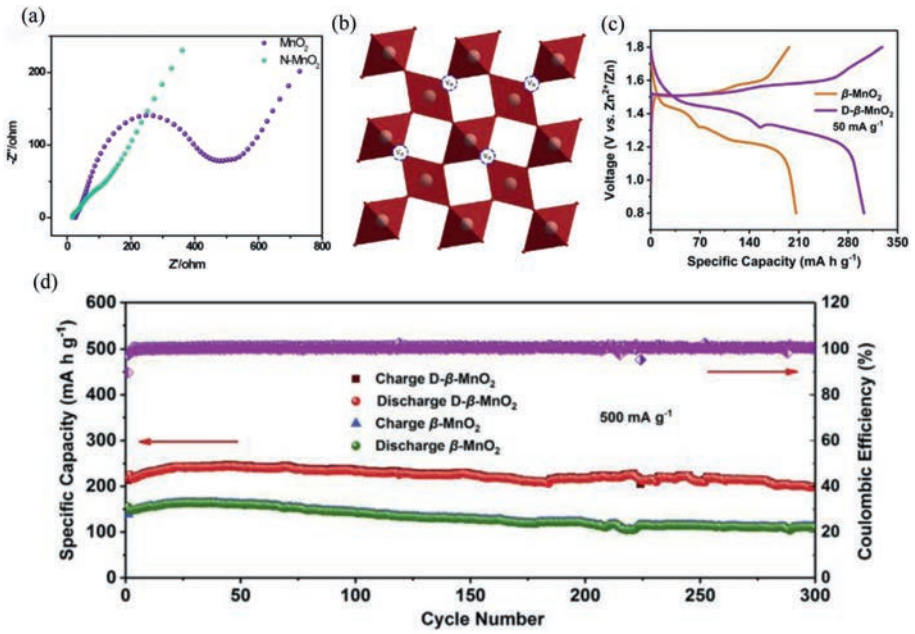


**Fig. 4.** (a) Nyquist plots for Zn/$MnO_2$ and Zn/N-$MnO_2$ battery. Reproduced with permission [39]. Copyright 2018, World Scientific Publishing. (b) Crystal structure of rutile-type $\beta$-$MnO_2$. (c) GCD profiles at 50 mA/g. (d) Cycling performances at 500 mA/g. Reproduced with permission [41]. Copyright 2020, Elsevier B.V.

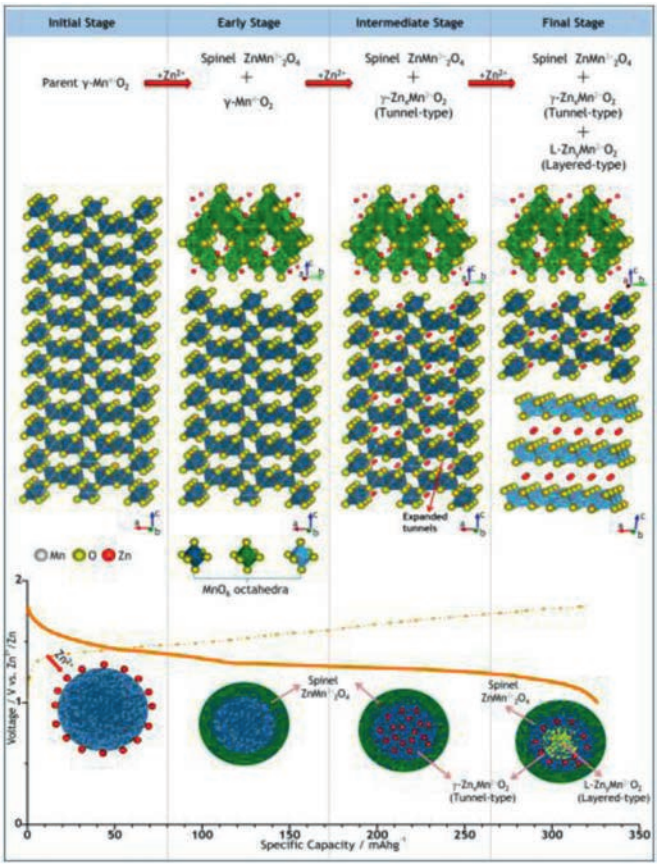


**Fig. 5.** Schematic of the reaction pathway of Zn-insertion in the prepared $\gamma$-$MnO_2$ cathode. Reproduced with permission [43]. Copyright 2015, American Chemical Society.

up the migration speed of $Zn^{2+}$. Fig. 6g shows two stages electrochemical reaction process: $H^+$ intercalation and $Zn^{2+}$ intercalation. When Zn ions intercalation begin, the host material changes from a tunnel structure to a layered $Zn_yH_xK_{0.19}MnO_2$. K ions play a key role in supporting structure. Therefore, Zn/$\alpha$-$K_{0.19}MnO_2$ battery exhibits a superior rate performance and delivers a capacity of 113 mAh/g at 20 C (Fig. 6f) [47].

Three chains composed of $MnO_6$ octahedrons are arranged into a 3 × 3 large tunnels to form todorokite $MnO_2$ (T-$MnO_2$) as shown in Fig. 3d. Because of the abundant tunnel space, various cations and water molecules can be easily accommodated in host framework. Therefore, theoretically, their cycle performance and rate performance are better than traditional 2 × 2 tunnel structure. Lee *et al.* discovered that T-$MnO_2$ is a potential cathode material used in ZIBs. Then they studied the behavior of zinc ions embedded in tunnel structure. In fact, the formation of large tunnel is usually through the expansion of $MnO_6$ layers and ion exchange. In addition, more ions and water molecules in tunnel can ensure the stability of structure during reaction process and provide more space for Zn ions migration [48].

### 2.2. Layered structure

$\delta$-$MnO_2$ is a layered structure material with a large interlayer spacing of 7.0 Å (Fig. 3e) [49,50]. Kim *et al.* prepared $\delta$-$MnO_2$ nanoflakes with an initial discharge capacity of 122 mAh/g. In the discharge process, spinel-type $ZnMn_2O_4$ appears. It indicates that layered $MnO_2$ undergoes a structural transformation. Moreover, some irreversible phases (MnOOH, $Mn(OH)_2$, $Mn_3O_4$ and $Mn_2O_3$) could be also observed [51]. Among them, MnOOH is a new material produced by the conversion reaction between $\delta$-$MnO_2$ and $H^+$, as shown in the following formulas.

$$H_2O \leftrightarrow H^+ + OH^- \quad (1)$$

$$MnO_2 + H^+ + e^- \leftrightarrow MnOOH \quad (2)$$

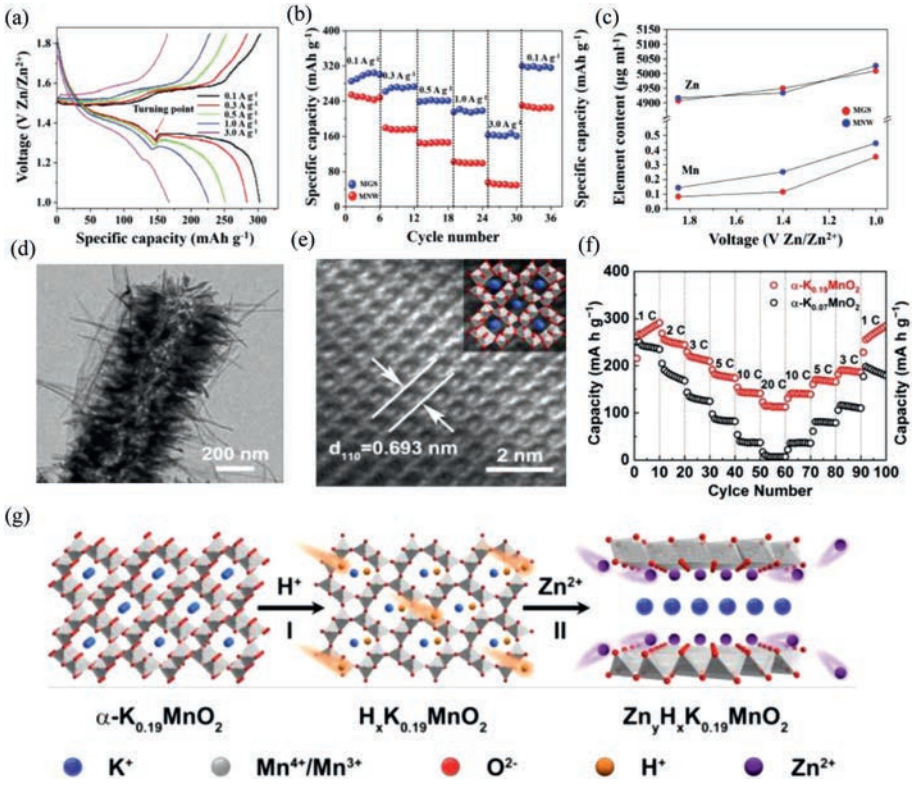


**Fig. 6.** (a) GCD curves of sample at current densities ranging from 0.1 A/g to 3 A/g. (b) Rate performances of samples. (c) Element analysis of $Zn^{2+}$ and dissolved $Mn^{2+}$ in a 2 mol/L $ZnSO_4$ aqueous electrolyte during the discharge process of first cycle. Reproduced with permission [46]. Copyright 2018 Wiely-VCH. (d) TEM images, (e) HRTEM image, (f) rate performance, (g) schematic of $H^+/Zn^{2+}$ intercalation processes in $\alpha$-$K_{0.19}MnO_2$ nanotubes. Reproduced with permission [47]. Copyright 2019, The Royal Society of Chemistry.

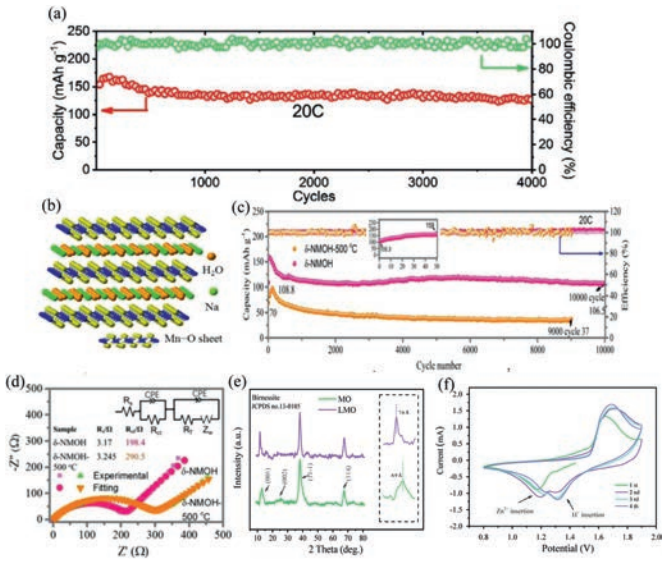


**Fig. 7.** (a) The cycle performance of Zn-$\delta$-$MnO_2$ battery. Reproduced with permission [52]. Copyright 2019, Wiely-VCH. (b) Structural illustration of the as-prepared Na ion and water molecule intercalated layered $\delta$-$MnO_2$ electrode. (c) The long-term cycling stability of electrodes at 20 C, with the inset showing the activation process within 50 cycles. (d) EIS curves. Reproduced with permission [53]. Copyright 2019, American Chemical Society. (e) XRD patterns. (f) CV curves at 1 mV/s. Reproduced with permission [54]. Copyright 2019, The Royal Society of Chemistry.

The formation of these by-products exerts a certain effect on the electrochemical performance of battery. Nevertheless, the battery still delivers a discharge capacity of 136.9 mAh/g at an operating rate of 20 C. It keeps a capacity retention of 93% after 4000 cycles (Fig. 7a) [52]. $\delta$-$MnO_2$ can transform to other crystal forms during reaction, resulting in a large volume change and structural collapse, which is the main reason to the poor cycle stability. Zhi's group pre-embedded $Na^+$ and water molecules into $\delta$-$MnO_2$ structure in order to stabilize host structure (Fig. 7b). To study the influence of structural water, cathode material powder was thermally treated at 500 °C. Fig. 7c presents the cycling performance of two electrodes at 20 C. It is found that Zn/$\delta$-$MnO_2$ with water molecule exhibits an ultra-stable cycle performance (98% of the initial capacity after 10000 cycles).

EIS curves (Fig. 7d) further confirmed that $R_{ct}$ of electrode without structural water increased significantly. The lack of water molecules makes a small amount of $Na^+$ unable to support the structural framework and reduces the transfer speed of $Zn^{2+}$. It greatly compromises the specific capacity and stability of device [53]. Zhang *et al.* developed an expanded layer interval strategy by rare earth La doping. The shift of XRD pattern confirms the expansion of interlayer spacing, which is conducive to the transmission of $Zn^{2+}$ (Fig. 7e). In addition, CV curves indicate that the doped $MnO_2$ electrodes possess high electrochemical reactivity (Fig. 7f). It means that the intercalation of $La^{3+}$ makes the transmission speed of Zn ions fast. The assembled device exhibits an energy density of 375.9 Wh/kg [54]. Related work has been reported successively such as $Co^{2+}$ [55], $Ca^{2+}$ [56], $V^{5+}$ [31] and rare earth element $Ce^{3+}$ [57]. The intercalation cations mainly play two roles: the first is to increase the interlayer spacing of host material and reduce the resistance of $Zn^{2+}$ insertion/extraction. The second is as the pillar of interlayer structure preventing the collapse of $\delta$-$MnO_2$ structure.

### 2.3. Spinel structure

Manganese-based oxides with spinel structure can be classified into the following types: $\lambda$-$MnO_2$ (Fig. 3f), $Mn_3O_4$ and $ZnMn_2O_4$.

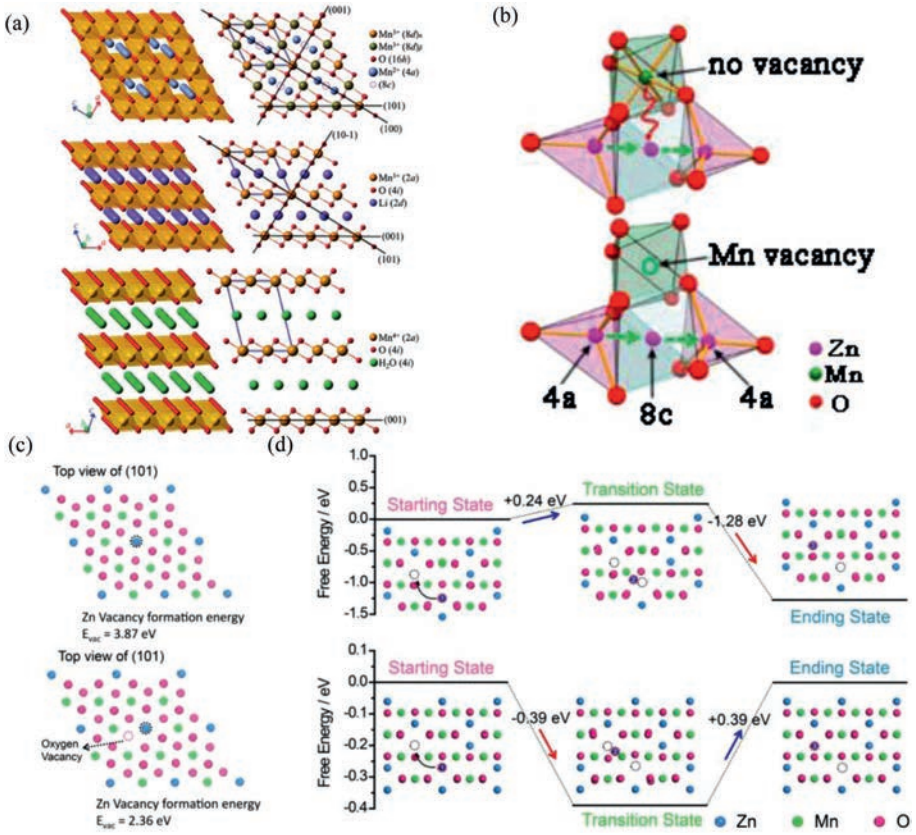


**Fig. 8.** (a) The crystal structure of $Mn_3O_4$ (spinel), $LiMnO_2$ (layered structure) and $MnO_2{\cdot}\gamma H_2O$ (Birnessite). Reproduced with permission [59]. Copyright 2015, Wiley-VCH. (b) $Zn^{2+}$ diffusion pathway in ZMO spinel without and with Mn vacancies. Reproduced with permission [64]. Copyright 2016, American Chemical Society. (c) Calculated structures of Zn vacancy formation energies ($E_{vac}$) of ZMO and OD-ZMO. (d) Energy profiles of Zn diffusion within ZMO and OD-ZMO. Reproduced with permission [65]. Copyright 2018, Elsevier B.V.

The internal space of the structure is not suitable for the insertion of $Zn^{2+}$ due to high electrostatic repulsion.

The layered manganese oxide with unstable structure can spontaneously undergo a phase transition from a layered to a spinel structure. It might be attributed to the preferential migration of Mn, which is related to the inherent characteristics of Mn [58]. However, Choi's group found that spinel $Mn_3O_4$ was transformed into layered Birnessite $A_xMnO_2{\cdot}yH_2O$ during cycling. Fig. 8a shows the crystal structure of $Mn_3O_4$ and other materials. It is found that spinel and layered type show a common structural basis of ABC-packed array with oxygen atoms. Therefore, phase change can be achieved without disturbing oxygen skeleton [59]. Besides, a binder-free SSWM@$Mn_3O_4$ electrode was prepared by Zhu and coworkers. The electrode directly grown on the substrate possesses a high conductivity, so Zn/SSWM@$Mn_3O_4$ battery delivers an excellent specific capacity and long cycle stability [60].

$ZnMn_2O_4$ materials with a spinel structure were first discovered in 2016. Shi *et al.* synthesized $Ti_3C_2T_x$ stabilized $ZnMn_2O_4$ nanoparticles (ZMO@ $Ti_3C_2T_x$). $Ti_3C_2T_x$ is a layered material with high conductivity. The composite materials can effectively prevent the irreversible structural degradation of ZMO and the occurrence of side reactions. Benefiting from the synergistic effect, the device can still maintain 92.4% of initial capacity after 5000 cycles [61]. Defect engineering is considered to be a suitable strategy to investigate the electrochemical activity of electrode materials [62]. It can be classified into four types: cation doping, oxygen vacancy, cation vacancy and anionic doping [63]. Recently, Zhang and colleagues reported cation-defective $ZnMn_2O_4$ materials as cathode for AZIBs. The device can deliver a discharge capacity of 150 mAh/g at 50 mA/g and durable long-term cycle ability. The mild synthesis conditions make the electrode structure rich in Mn ion vacancies. As shown in Fig. 8b, the formation of Mn ion vacancies reduces the electrostatic repulsion of Zn ions, leading to a rapid kinetic process [64].

Anion vacancies can also present a similar effect. The annealed $ZnMn_2O_4$ enriches oxygen vacancies and wraps a layer of conductive polymer PEDOT to improve conductivity. In Figs. 8c and d, DFT calculations suggest that the electrode containing oxygen defects shows a low energy barrier during the migration of zinc ions. It indicates that anion defect enhances the transfer speed of zinc ions in the structure. Therefore, the synergy of oxygen vacancies and PEDOT leads to the transition of $ZnMn_2O_4$ from semiconducting to conducting, which explains the significant increase in charge transport efficiency [65].

The electrochemical performance of various Mn-based compounds is listed in Table 1. It can be found the specific capacities of electrodes has been improved. Among them, $MnO_2$ with oxygen defects show a capacity of 345 mAh/g at 0.2 A/g [66]. The cycle number of Zn/$MnO_2$ batteries can reach 10000 cycles and maintain a retention of 99% [17]. In addition, these Mn-based materials show a common feature that the voltage window is basically maintained at 1–1.9 V. However, Qiao's group proposed a novel electrolytic Zn-$MnO_2$ batteries, which deliver a high voltage window (1.99 V) and achieve an energy density of 409 Wh/kg [67]. Energy density is a significant parameter to study the electrochemical performance of batteries. Compared to V-based compounds and Prussian blue analogs, manganese-based compounds have a high energy density. In Table 1, Zn/$O_d$-$MnO_2$ devices can exhibit an energy density of 470 Wh/kg.

**Table 1.**
The electrochemical performance of various Mn-based materials as cathode for aqueous ZIBs.

| Materials | Potential window (V) | Specific capacity (mAh/g)/Current density | Cyclic stability | Energy density (Wh/kg) | Ref. |
|---|---|---|---|---|---|
| $MnO_2$ | 1.0–1.8 | 290, 0.3C | ~99%, 10000 cycles, 6.5 C | – | [17] |
| V-doped $MnO_2$ | 1.0–1.8 | 266, 66 mA/g | 131 mAh/g, 100 cycles, 66 mA/g | – | [31] |
| $\beta$-$MnO_2$ | 1.0–1.9 | 355, 0.1 A/g | 110 mAh/g, 1000 cycles, 0.2 A/g | – | [38] |
| $\gamma$-$MnO_2$ | 0.8–1.8 | 285, 0.05 mA/cm$^2$ | 158 mAh/g, 40 cycles, 0.5 mA/cm$^2$ | | [43] |
| $MnO_2$/graphene | 0.8–1.8 | 301, 0.5 A/g | 64.1%, 300 cycles, 10 A/g | 411.6 | [44] |
| $\alpha$-$MnO_2$ | 1.0–1.85 | 285, C/3 | 92%, 5000 cycles, 5 C | ~170 | [45] |
| $\alpha$-$MnO_2$/graphene scrolls | 1.0–1.85 | 382.2, 0.3 A/g | 94%, 3000 cycles, 3 A/g | 406.6 | [46] |
| $\delta$-$MnO_2$ | 1–1.8 | 238.8, 0.2 C | 93%, 4000 cycles, 20 C | – | [52] |
| $Na_{0.44}Mn_2O_4{\cdot}1.5H_2O$ | 0.9–1.9 | 278, 1 C | 98%, 10000 cycles, 20 C | 374 | [53] |
| $Ca_{0.28}MnO_2{\cdot}0.5H_2O$ | 0.4–1.9 | 298, 175 mA/g | 100%, 5000 cycles, 3500 mA/g | – | [56] |
| $Mn_3O_4$ | 0.9–1.8 | 296, 0.1 A/g | 100%, 500 cycles, 0.5 A/g | – | [60] |
| $ZnMn_2O_4$ | 0.8–1.9 | ~150, 50 mA/g | 94%, 500 cycles, 0.5 A/g | 70 | [64] |
| $O_d$-$MnO_2$ | 1–1.8 | 345, 0.2 A/g | 84%, 2000 cycles, 5 A/g | 470 | [66] |
| $MnO_2$ | 0–1.99 | 570 | 92%, 1800 cycles, 30 mA/cm$^2$ | ~409 | [67] |

## 3. Energy storage mechanism

Mn-based compounds have obtained rapid development in the field of ZIBs, but there have been controversies on the energy storage mechanism. It is generally believed that there are four mechanisms: $Zn^{2+}$ insertion/extraction, chemical conversion reaction, dissolution-deposition mechanism and dual-ions insertion/extraction mechanism.

### 3.1. $Zn^{2+}$ insertion/extraction mechanism

$Zn^{2+}$ is (de-)intercalated between cathode and anode. Since zinc ions are intercalated into cathode, $MnO_2$ is transformed into spinel structure $ZnMn_2O_4$ [68]. During the charge process, the new phase is transformed back into the original material. Additionally, Mn vacancies are introduced to form defects to increase the conductivity of host material. At the same time, DFT calculations show that the existence of Mn vacancies can stabilize the structure of electrode when zinc ions are intercalated as shown in Fig. 9a. It indicates that MnO materials with defects easily accommodate the transfer of Zn ion. The *ex-situ* XRD patterns (Fig. 9b) reveal the kinetic reaction process of battery without the appearance of other impurities. It ensures superior electrochemical performance of battery. The reaction process of $Zn^{2+}$ (de-)intercalation can be described by following formula (Fig. 9c) [69].

$$MnO \rightarrow Mn_{0.61}O + 0.39\ Mn^{2+} + 0.78\ e^{-}\ (1^{st}) \quad (3)$$

$$Mn_{0.61}O + yZn^{2+} + 2ye^{-} \leftrightarrow Zn_yMn_{0.61}O\ (\text{further cycle}) \quad (4)$$

### 3.2. Conversion reaction mechanism

Electrochemical conversion mechanism induced by hydrogen ion has also been reported recently [45,70]. For instance, Liu's group proposed a chemical conversion reaction that effectively improves the electrochemical performance of device. And a series of characterization methods confirmed the reaction process of $H^+$ insertion, which can be summarized as [45]:

$$MnO_2 + H^+ + e^{-} \leftrightarrow MnOOH \quad (5)$$

$$2MnO_2 + Zn^{2+} + 2e^{-} \leftrightarrow ZnMn_2O_4 \quad (6)$$

The reaction also occurs in $Zn/MnO_2$ batteries. During the reaction, the by-product $Zn(OH)_2)_3ZnSO_4{\cdot}xH_2O$ (ZSH) is generated on the surface of cathode material due to the insertion of $H^+$ (formula 7). When charging, $H^+$ is released from host structure and ZSH dissolves [71].

$$2Zn^{2+} + 6OH^{-} + SO_4{}^{-2} + xH_2O \rightarrow Zn(OH)_2)_3ZnSO_4{\cdot}xH_2O \quad (7)$$

### 3.3. Dissolution-deposition mechanism

Based on the above reaction process, a new type dissolution-deposition mechanism is proposed [72,73]. Guo and co-workers studied the effect of ZHS and birnessite-$MnO_2$ product on the capacity loss and manganese dissolution process. In Fig. 9d, ZSH layer gradually generated during the second cycle discharging. It can effectively prevent the dissolution of Mn, thereby increasing the capacity of device. Generally speaking, the energy storage process can be divided into two parts. As shown in Fig. 9e, the formation of ZHS and the dissolution of Mn ions occur in the first cycle of discharge (formula 8). The first cycle of charge forms a new phase birnessite-$MnO_2$ (formula 9). In the subsequent cycles, birnessite-$MnO_2$ restored to the original phase, and the reaction is repeated continuously. Therefore, the high reversibility of $Zn/MnO_2$ battery can deliver a stable capacity [73].

$$3MnO_2 + 6H_2O + 6e^{-} \rightarrow 3Mn^{2+} + 12OH^{-} \quad (8)$$

$$3Mn^{2+} + 12OH^{-} \rightarrow 3\ \text{birnessite-}MnO_2 + 6H_2O + 6e^{-} \quad (9)$$

### 3.4. Dual-ions insertion/extraction mechanism

Researchers have been developing new storage mechanisms that are conducive to enhancing the electrochemical performance of cathode. This dual ion intercalation mechanism includes two classifications: the co-intercalation and extraction of non-metallic ions or metal ions and $Zn^{2+}$. Recently, $H^+$ and $Zn^{2+}$ co-insertion/extraction mechanism are frequently reported in Mn-based compounds for AZIBs [74–76]. Xia's group designed a PANI-intercalated $MnO_2$ electrode. The reaction process of device includes four processes according to charging and discharging mechanism. The initial stage of discharging is the insertion of $H^+$. The second discharge plateau is related to the insertion of $Zn^{2+}$ [75]. Similarly, Sun *et al.* found that GCD curves of $Zn/MnO_2$ @CFP battery possess two plateau regions (Fig. 10a). The capacity decay speed of these two parts is obviously different. Moreover, the charge diffusion resistance presents a significant difference (Fig. 10b). This may be caused by various ion insertions. *Ex-situ* XRD (Fig. 10c) further confirmed that the typical MnOOH peaks appeared after discharging to 1.3 V due to the insertion of $H^+$. When the electrode was further discharged to 1.0 V, the diffraction peaks of $ZnMn_2O_4$ disappeared [17].

Manganate electrodes are also suitable for this charge storage mechanism. Liang's group designed $K_{0.8}Mn_8O_{16}$ electrode with

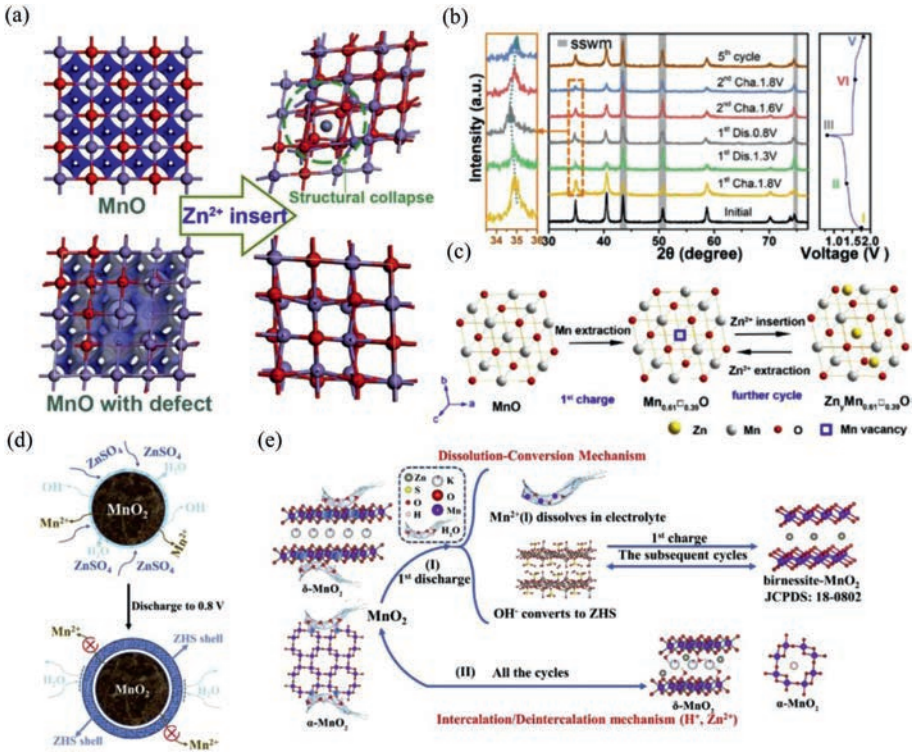


**Fig. 9.** (a) Charge distribution of MnO and $Mn_{0.61}\square_{0.39}O$, and the structures after $Zn^{2+}$ insertion. (b) The *ex-situ* XRD patterns and corresponding GCD curves at 0.1 A/g. (c) Schematic of $Zn^{2+}$ insertion/extraction in a MnO framework. Reproduced with permission [69]. Copyright 2019, Elsevier B.V. (d) The schematic of the role of ZHS in the discharge process. (e) The schematic of energy storage mechanism in $Zn/MnO_2$ battery. Reproduced with permission [73]. Copyright 2020, Elsevier B.V.

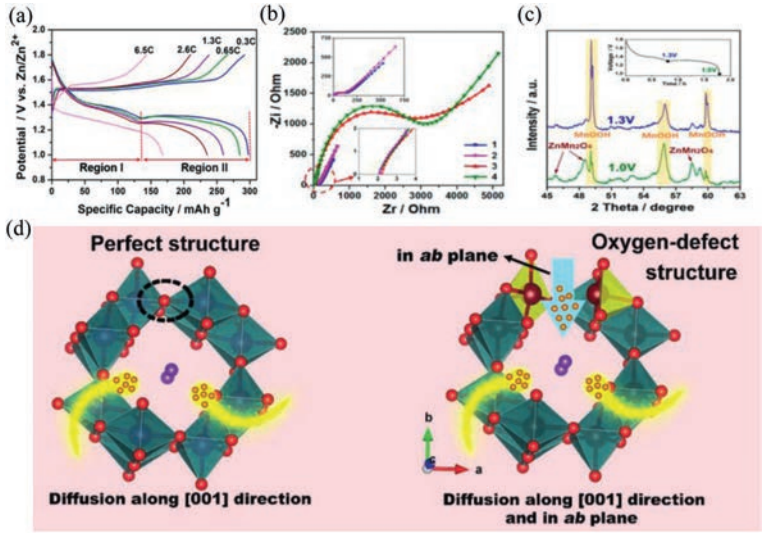


**Fig. 10.** (a) GCD curves of $MnO_2$@CFP at different rates in first cycle. (b) EIS curves. (c) *Ex-situ* XRD patterns at depth of discharge at 1.3 and 1.0 V, respectively. Reproduced with permission [17]. Copyright 2017, American Chemical Society. (d) Schematic of $H^+$ diffusion into KMO with perfect structure and oxygen-defect structure. Reproduced with permission [37]. Copyright 2019, Wiley-VCH.

oxygen defects. $K^+$ is added to inhibit the dissolution of manganese, thereby ensuring the structural stability of manganese-based cathode. The introduction of oxygen defects prompts $MnO_6$ polyhedral wall open, which is conducive to the diffusion of $H^+$ in the ab-plane (Fig. 10d). Therefore, the electrochemical reaction activity and reaction kinetics of KMO are improved. Zn/$K_{0.8}Mn_8O_{16}$ (KMO) batteries show an energy density of 398 Wh/kg based on the intercalation mechanism of $Zn^{2+}$ and $H^+$ [37]. Zhai and co-workers prepared $Na_{0.55}Mn_2O_4{\cdot}0.57H_2O$ (NMOH) cathodes and proposed an electrochemical mechanism for the co-intercalation of $Na^+$ and crystal water. Fig. 11 shows that Zn ion (de-)intercalated reaction mechanism. During the discharging process, $H^+$ first enters NMOH structures and produces by-products $Zn_4SO_4(OH)_6{\cdot}0.5H_2O$. Then Zn ions intercalate to replace a small part of sodium ions supporting the main structure.

This sequential embedding process indicates a two-step reaction process. Finally, Zn ions are released from layer structure during the charging state. The continuous insertion and extraction of $H^+$ and $Zn^{2+}$ are accompanied by $Na^+$ desorption. This replace-

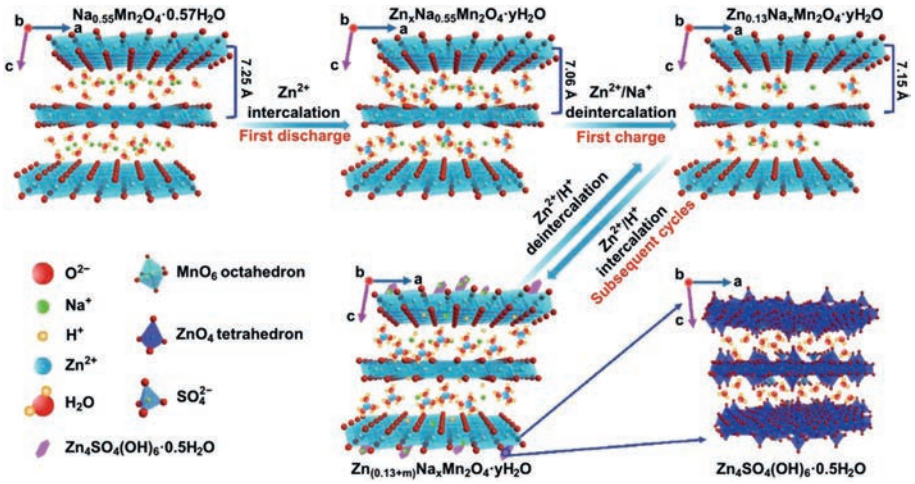


**Fig. 11.** Schematic of the displacement/intercalation reaction mechanism in the first cycle, and the insertion/extraction mechanism of zinc ions in subsequent electrochemical discharge/charge processes. Reproduced with permission [77]. Copyright 2020, Springer.

ment/intercalation reaction mechanism makes Zn/NMOH batteries exhibit a specific capacity of 389.8 mAh/g at 0.2 A/g and excellent cycle performance [77].

Soundharrajan *et al.* constructed a novel Zn/$MgMn_2O_4$ battery, which kept a capacity retention of 80% after 500 cycles. In order to prevent the inert diffusion of magnesium ions in the crystal lattice, electrolyte is modified to a certain extent. The assembled devices confirm the existence of two pairs of redox peaks through CV curves. It could be due to the gradual insertion of $Zn^{2+}/Mg^{2+}$ into the spinel structure. The following reactions could occur during the cycle process:

$$MgMn_2O_4 + xe^- \rightarrow Mg_{(1-x)}Mn_2O_4 + xMg^{2+} \quad (10)$$

$$Mg_{(1-x)}Mn_2O_4 + yMg^{2+} + (x-y)Zn^{2+} \leftrightarrow Mg_{[(1-x)+y]}Zn_{(x-y)}Mn_2O_4 + xe^- \quad (11)$$

Beneficial to the mechanism of $Zn^{2+}/Mg^{2+}$ co-insertion and extraction, the devices achieve an energy density of 370 Wh/kg at 70 W/kg [78].

## 4. Conclusion and perspective

In summary, $MnO_2$ have become promising cathode materials for ZIBs due to their rich crystal structures. This review summarizes recent advances of manganese-based oxides electrode materials and emphasizes the effect of different synthesis strategies on performance of cathode materials. In addition, several electrochemical mechanisms of Zn/Mn-based battery are introduced. Mn-based materials have been explored for a long time, there are still some key problems that have not been resolved. Firstly, the performance of batteries is far from meeting market requirements. Therefore, it has a long way to achieve high electrochemical performance of AZIBs batteries. One should continue to develop and design some new synthetic strategies by tailoring morphology, specific surface area and crystal structure of electrode materials. Increasing ion conductivity and the surface area can promote $Zn^{2+}$ ion diffusion coefficient and enhance the surface capacitance behavior.

Secondly, manganese dioxide is prone to irreversible structural phase change and accompanied by the dissolution of Mn ions during reaction. Thus, it leads to a decline in capacity and reduce in cyclic life. Therefore, some general strategies might be employed: (1) Adding a small amount of solution with $Mn^{2+}$ to the electrolyte to ensure the stability of electrode. (2) The use of a weakly acidic electrolyte such as $Zn(CF_3SO_3)_2$ can inhibit the dissolution of $Mn^{2+}$. Moreover, it is also a good strategy to develop new electrolyte additives to protect the electrode/electrolyte interface by forming a dense passivation film. Besides, carbon coating, defect engineering and conductive polymer coating are also used to modulate the electrode structure.

Finally, the voltage window of manganese-based battery is relatively low. Therefore, it is necessary to broaden the voltage window by optimizing cathode structure. Most of literature use novel electrolytes to achieve the purpose of increasing the voltage window, such as high-concentration salt, new electrolyte additives (0.1 mol/L $H_2SO_4$). Furthermore, it is also a feasible strategy to explore the redox reaction mechanism of multivalent electrons such as $Mn^{4+}/Mn^{2+}$.

## Declaration of competing interest

The authors declare no conflict of interest.

## Acknowledgements

This work was supported by the Opening Project of State Key Laboratory of High Performance Ceramics and Superfine Microstructure (No. SKL201904SIC), State Key Laboratory of Advanced Technology for Materials Synthesis and Processing (Wuhan University of Technology) (No. 2020-KF-12) and the Opening Project of State Key Laboratory of Metastable Materials Science and Technology (No. 202007).

## References

[1] Y. Gogotsi, P. Simon, Science 334 (2011) 917–918.
[2] D.P. Zhao, M.Z. Dai, Y. Zhao, et al., Nano Energy 72 (2020) 104715.
[3] L.J. Su, L.Y. Liu, Y. Wang, Y.L. Lu, X.B. Yan, Chin. Chem. Lett. 31 (2020) 2358–2364.
[4] X. Wu, S.Y. Yao, Nano Energy 42 (2017) 143–150.
[5] J.M. Tarascon, M. Armand, Nature 414 (2001) 359–367.
[6] C. Liu, X. Wu, B. Wang, Chem. Eng. J. 392 (2020) 123651.
[7] H. Yuan, L. Kong, T. Li, Q. Zhang, Chin. Chem. Lett. 28 (2017) 2180–2194.
[8] M. Song, H. Tan, D. Chao, H.J. Fan, Adv. Funct. Mater. 28 (2018) 1802564.
[9] Y.Q. Qi, Y. Yang, Q. Hou, et al., Chin. Chem. Lett. 32 (2021) 1117–1120.
[10] W. Fang, R. Jiang, H. Zheng, et al., Rare Metals 40 (2020) 433–439.
[11] G.A. Elia, K. Marquardt, K. Hoeppner, et al., Adv. Mater. 28 (2016) 7564–7579.
[12] Z. Yan, Q.W. Yang, Q. Wang, J. Ma, Chin. Chem. Lett. 31 (2020) 583–588.
[13] Y. Song, S. Jiao, J. Tu, et al., J. Mater. Chem. A 5 (2017) 1282–1291.
[14] Y. Liu, P.F. Hu, H.Q. Liu, X. Wu, C.Y. Zhi, Mater. Today Energy 17 (2020) 100431.
[15] B.Y. Tang, L.T. Shan, S.Q. Liang, J. Zhou, Energy Environ. Sci. 12 (2019) 3288–3304.
[16] Y. Liu, X. Wu, J. Energy Chem. 56 (2021) 223–237.

[17] W. Sun, F. Wang, S. Hou, et al., J Am. Chem. Soc. 139 (2017) 9775–9778.
[18] S. Bi, Y. Wu, A. Cao, et al., Mater. Today Energy (2020) 18.
[19] Y. Zhang, S. Deng, Y. Li, et al., Energy Storage Mater. 29 (2020) 52–59.
[20] Y. Liu, X. Wu, Nano Energy 86 (2021) 106124.
[21] Q. Li, X. Rui, D. Chen, et al., Nano Micro. Lett. 12 (2020) 67.
[22] F. Liu, Z. Chen, G. Fang, et al., Nano-Micro Lett. 11 (2019) 25.
[23] D. Chen, X. Rui, Q. Zhang, et al., Nano Energy 60 (2019) 171–178.
[24] Q. Yang, F. Mo, Z. Liu, et al., Adv. Mater. 31 (2019) e1901521.
[25] G. Kasiri, J. Glenneberg, A.B. Hashemi, R. Kun, F. La Mantia, Energy Storage Mater. 19 (2019) 360–369.
[26] P. Hu, T. Zhu, X. Wang, et al., Nano Energy 58 (2019) 492–498.
[27] V. Verma, S. Kumar, W. Manalastas, et al., ACS Appl. Energy Mater. 2 (2019) 8667–8674.
[28] T. Yamamoto, T. Shoji, Inorg. Chim. Acta 117 (1986) L27–L28.
[29] X. Zeng, J. Hao, Z. Wang, J. Mao, Z. Guo, Energy Storage Mater. 20 (2019) 410–437.
[30] J. Huang, J. Zeng, K. Zhu, R. Zhang, J. Liu, Nano-Micro Lett. 12 (2020) 110.
[31] M.H. Alfaruqi, S. Islam, V. Mathew, et al., Appl. Surf. Sci. 404 (2017) 435–442.
[32] B. Jiang, C. Xu, C. Wu, et al., Electrochim. Acta 229 (2017) 422–428.
[33] D. Xu, B. Li, C. Wei, et al., Electrochim. Acta 133 (2014) 254–261.
[34] J. Ming, J. Guo, C. Xia, W. Wang, H.N. Alshareef, Mater. Sci. Eng. R: Rep. 135 (2019) 58–84.
[35] V. Soundharrajan, B. Sambandam, S. Kim, et al., Energy Storage Mater 28 (2020) 407–417.
[36] X. Wu, Y. Li, C. Li, et al., J. Power Sources 300 (2015) 453–459.
[37] G. Fang, C. Zhu, M. Chen, et al., Adv. Funct. Mater. 29 (2019) 1808375.
[38] W. Liu, X. Zhang, Y. Huang, et al., J. Energy Chem. 56 (2021) 365–373.
[39] Y. Huang, W. He, P. Zhang, X. Lu, Funct. Mater. Lett. 11 (2018) 1840006.
[40] N. Zhang, X. Li, H. Ye, et al., J. Am. Chem. Soc. 138 (2016) 8928–8935.
[41] M. Han, J. Huang, S. Liang, et al., iScience 23 (2020) 100797.
[42] Y. Zou, W. Zhang, N. Chen, et al., ACS Nano 13 (2019) 2062–2071.
[43] M.H. Alfaruqi, V. Mathew, J. Gim, et al., Chem. Mater. 27 (2015) 3609–3620.
[44] C. Wang, Y.X. Zeng, X. Xiao, et al., J. Energy Chem. 43 (2020) 182–187.
[45] H.L. Pan, Y.Y. Shao, P.F. Yan, et al., Nat. Energy 1 (2016) 16039.
[46] B.K. Wu, G.B. Zhang, M.Y. Yan, et al., Small 14 (2018) 1703850.
[47] G. Liu, H. Huang, R. Bi, et al., J. Mater. Chem. A 7 (2019) 20806–20812.
[48] J. Lee, J.B. Ju, W.I. Cho, B.W. Cho, S.H. Oh, Electrochim. Acta 112 (2013) 138–143.
[49] M. Nakayama, T. Kanaya, J.W. Lee, B.N. Popov, J. Power Sources 179 (2008) 361–366.
[50] A.A. Voskanyan, C.K. Ho, K.Y. Chan, J. Power Sources 421 (2019) 162–168.
[51] M.H. Alfaruqi, J. Gim, S. Kim, et al., Electrochem. Commun. 60 (2015) 121–125.
[52] Y. Jin, L. Zou, L. Liu, et al., Adv. Mater. 31 (2019) e1900567.
[53] D. Wang, L. Wang, G. Liang, et al., ACS Nano 13 (2019) 10643–10652.
[54] H. Zhang, Q. Liu, J. Wang, et al., J. Mater. Chem. A 7 (2019) 22079–22083.
[55] Y. Zhong, X. Xu, J.P. Veder, Z. Shao, iScience 23 (2020) 100943.
[56] T. Sun, Q. Nian, S. Zheng, J. Shi, Z. Tao, Small 16 (2020) e2000597.
[57] J. Wang, X. Sun, H. Zhao, et al., J. Phys. Chem. C 123 (2019) 22735–22741.
[58] W. Xu, Y. Wang, Nano-Micro Lett. 11 (2019) 90.
[59] S. Kim, K.W. Nam, S. Lee, et al., Angew. Chem. Int. Ed. 54 (2015) 15094–15099.
[60] C. Zhu, G. Fang, J. Zhou, et al., J. Mater. Chem. A 6 (2018) 9677–9683.
[61] M. Shi, B. Wang, Y. Shen, et al., Chem. Eng. J. 399 (2020) 125627.
[62] C. Xie, D. Yan, W. Chen, et al., Mater. Today 31 (2019) 47–68.
[63] T. Xiong, Y. Zhang, W.S.V. Lee, J. Xue, Adv. Energy Mater. 10 (2020) 2001769.
[64] N. Zhang, F. Cheng, Y. Liu, et al., J. Am. Chem. Soc. 138 (2016) 12894–12901.
[65] H. Zhang, J. Wang, Q. Liu, et al., Energy Storage Mater. 21 (2019) 154–161.
[66] T. Xiong, Z.G. Yu, H. Wu, et al., Adv. Energy Mater. 9 (2019) 1803815.
[67] D.L. Chao, W.H. Zhou, C. Ye, et al., Angew. Chem. Int. Ed. 58 (2019) 7823–7828.
[68] M.H. Alfaruqi, J. Gim, S. Kim, et al., J. Power Sources 288 (2015) 320–327.
[69] C. Zhu, G. Fang, S. Liang, et al., Energy Storage Mater. 24 (2020) 394–401.
[70] B. Lee, H.R. Seo, H.R. Lee, et al., ChemSusChem 9 (2016) 2948–2956.
[71] J. Wang, J.G. Wang, H. Liu, C. Wei, F. Kang, J. Mater. Chem. A 7 (2019) 13727–13735.
[72] G. Liang, F. Mo, H. Li, et al., A, Adv. Energy Mater. 9 (2019) 1901838.
[73] X. Guo, J. Zhou, C. Bai, et al., Mater. Today Energy 16 (2020) 100396.
[74] X. Gao, H. Wu, W. Li, et al., Small 16 (2020) e1905842.
[75] J. Huang, Z. Wang, M. Hou, et al., Nat. Commun. 9 (2018) 2906.
[76] C. Guo, Q.H. Zhou, H.M. Liu, et al., Electrochim. Acta 324 (2019) 134867.
[77] X.Z. Zhai, J. Qu, S.M. Hao, et al., Nano-Micro Lett. 12 (2020) 56.
[78] V. Soundharrajan, B. Sambandam, S. Kim, et al., ACS Energy Lett. 3 (2018) 1998–2004.